PAPER

Influence of sheet resistance and strip width on the detection efficiency saturation in micron-wide superconducting strips and large-area meanders

IOP Publishing Superconductor Science and Technology
Supercond. Sci. Technol. **34** (2021) 084001 (8pp) https://doi.org/10.1088/1361-6668/ac0950

Influence of sheet resistance and strip width on the detection efficiency saturation in micron-wide superconducting strips and large-area meanders

Yu P Korneeva[1,*], N N Manova[1], M A Dryazgov[1,2], N O Simonov[1], Ph I Zolotov[1,2,3] and A A Korneev[1,2]

[1] Moscow Pedagogical State University, 1 Malaya Pirogovskaya str., Moscow 119991, Russia
[2] National Research University Higher School of Economics, 20 Myasnitskaya, Moscow 101000, Russia
[3] LLC Superconducting Nanotechnology (SCONTEL), Moscow 119021, Russia

E-mail: korneeva_yuliya@mail.ru

Received 18 January 2021, revised 21 April 2021
Accepted for publication 8 June 2021
Published 28 June 2021

Abstract

We report our study of detection efficiency (DE) saturation in wavelength range 400–1550 nm for the NbN superconducting microstrip single-photon detectors (SMSPDs) featuring the strip width up to 3 μm. We observe an expected decrease of the DE saturation plateau with the increase of photon wavelength and decrease of film sheet resistance. At 1.7 K temperature DE saturation can be clearly observed at 1550 nm wavelength in strip with the width up to 2 μm when sheet resistance of the film is above 630 $\Omega\,\mathrm{sq}^{-1}$. In such strips the length of the saturation plateau almost does not depend on the strip width. We used these films to make meander-shaped detectors with the light sensitive area from 20×20 $\mu\mathrm{m}^2$ to a circle 50 μm in diameter. In the latter case, the detector with the strip width of 0.49 μm demonstrates saturation of DE up to 1064 nm wavelength. Although DE at 1310 and 1550 nm is not saturated, it is as high as 60%. The response time is limited by the kinetic inductance and equals to 20 ns (by 1/*e* decay), timing jitter is 44 ps. When coupled to multi-mode fibre large-area meanders demonstrate significantly higher dark count rate which we attribute to thermal background photons, thus advanced filtering technique would be required for practical applications.

Keywords: superconducting thin films, single-photon detectors, detection efficiency

(Some figures may appear in colour only in the online journal)

1. Introduction

The superconducting (nanowire) single-photon detectors (SSPD or SNSPDs) [1] have become devices of choice in many advanced applications of quantum optics such as quantum cryptography and quantum computing. In these applications light at telecom wavelength 1550 nm can be delivered to the SNSPD by a single-mode optical fibre. The superior performance of SNSPD in terms of detection efficiency (MoSi [2] and NbN [3]), dark counts and timing resolution (jitter) [4] together with possibility to install several detectors in a single cryocooler make them commercially competitive with semiconducting single-photon avalanche diodes (SPADs). Meanwhile there are great many applications which would gain benefit from large-area detectors which could be

* Author to whom any correspondence should be addressed.

Table 1. Properties of the NbN films under study. R_s(300 K) is the film sheet resistance at $T = 300$ K; T_c is the critical temperature determined from the midpoint of the resistive transition; *RRR* is the residual resistance ration $R_s(300\text{ K})/R_s(20\text{ K})$; j_{dep} is the calculated depairing current density at $T = 1.7$K; $j_c/j_{dep}(1.7\text{ K})$ is the ratio of averaged over all straight strips $j_c(1.7\text{ K})$ measured without shunt resistor to $j_{dep}(1.7\text{ K})$.

Film ID	Sublayer	R_s(300 K), $\Omega\,\text{sq}^{-1}$	T_c, K	*RRR*	j_{dep}(1.7 K), $\mu\text{A}\,\mu\text{m}^{-1}$	j_c/j_{dep}	Thickness, nm
2347-1	SiO_2	753	8.0	0.57	137	0.71	5.4
2347-2	Si_3N_4	799	7.5	0.62	124	0.52	5.4
2373C	SiO_2	620	8.3	0.68	214	0.77	4.7
2415-2	Si_3N_4	550	9.0	0.72	285	0.85	5.7
2441	Si_3N_4	634	8.0	0.66	187	0.56	5.8
2474-1	Si_3N_4	636	9.3	0.73	264	0.64	3.7
2478	Si_3N_4	560	9.9	0.74	335	0.6	4.3
2479-1	Si_3N_4	625	8.2	0.66	198	0.54	5.2
2479-2	SiO_2	625	8.2	0.66	198	0.53	5.2
2486-1	Si_3N_4	544	9.5	0.75	328	0.62	4.6
2486-2	Si_3N_4	544	9.5	0.75	328	0.63	4.6
2647-4	Si_3N_4	585	8.9	0.72	263	0.45	4.9
2818	Si_3N_4	676	8.7	0.72	219	0.67	5.4

efficiently coupled to multi-mode fibres with 50 μm core diameter. Traditional SNSPDs with 100 nm-wide strip are not suitable for such purpose due to significant increase of kinetic inductance (let alone the drastic decrease of fabrication yield).

In Korneeva *et al* [5] we have demonstrated single-photon detection by micron-wide NbN strips. This effect had been predicted well before by Zotova and Vodolazov [6–8]. The model is based on numerical solution of time-dependent Ginzburg–Landau equations and predicts that if the bias current is sufficiently close to the depairing current I_{dep}, the photon absorption leads to the formation of vortex-antivortex pairs in the hot-spot. Movement of the vortexes leads to the Joule heating of the strip and destruction of superconductivity.

Recently it was demonstrated that NbN is not unique for single-photon detection in micron-wide strips: the effect was also observed in amorphous MoSi [9, 10] and WSi [11] films. In [12] over 90% saturated detection efficiency was shown for SMSPD fabricated from He ion pre-irradiated NbN film.

Here we present our recent progress in development of SMSPDs aimed at practical applications. We analysed a large amount of microstrip detectors fabricated from many NbN films with sheet resistance R_s in range from 550 to 800 $\Omega\,\text{sq}^{-1}$ trying to setup a correlation between R_s, strip width, wavelength and the possibility to achieve the saturation of the internal detection efficiency (IDE). Then we analyse the performance of microstrip meanders to estimate the ultimate characteristics of the practical detectors suitable for coupling to multi-mode fibres and light from free space. As the microstrip detectors feature smaller kinetic inductance they are more affected by 'latching' (i.e. superconductivity does not spontaneously restore after photon absorption and the device remains 'latched'). Thus the issue of counter-latching measures is important for practical applications. Usually additional inductance or shunt resistor are used to prevent latching. We analyse the influence of these counter-measures on the ultimate device characteristics.

2. Methods and samples under test

For our samples we use NbN films deposited by the same route as described in our previous work [5]. In brief, the films are deposited by DC reactive magnetron sputtering of Nb target in argon and nitrogen atmosphere. The thickness of the film is estimated by the deposition time and deposition rate. The latter is measured in a calibration process when thick film is deposited. As the thickness of a-few-nm-thick-film cannot be accurately defined, here we prefer to use sheet resistance as the major film characteristics which is inversely proportional to the film thickness given that we use the same residual nitrogen pressure for all studied films (we believe that this fact results in more or less the same stoichiometry of the produced films). The main properties of the fabricated films are summed up in table 1.

The films are patterned into straight strips and meanders using electron-beam lithography in PMMA electron resist. The entry and exit points of the strips and turns of the meanders have rounded edges according to [13] preventing current-crowding effect (as shown in the inset in figure 1). The widths of the strips varied in the range 0.2–3 μm. For the majority of the samples, the length is chosen 10 times of the width so that the samples are 10 squares long. All the fabricated samples passed initial screening at 4.2 K temperature: we measured IV-curves and selected the samples with the highest critical currents. Typically more than 60% of the samples are chosen for further study.

All further testing is performed at 1.7 K temperature in liquid-He-pumped cryoinsert for the storage dewar. Light from cw and pulsed lasers is coupled in SMF-28 fibre (single-mode for 1550 nm wavelength) and fed to low temperature part of the cryoinsert. The sample under test is located at a distance of several centimetres away from the pigtail of the fibre to provide a uniform illumination. The calibration of the setup for DE measurements is performed by direct measurement of light power and by measurement of a meander with

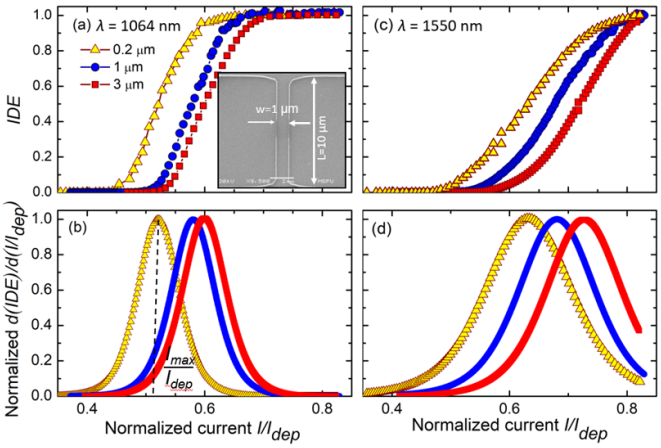

Figure 1. (a) A dependence of internal quantum efficiency IDE on normalized bias current ($I/I_{\rm dep}$) measured at 1064 nm wavelength for three strips with widths 0.2, 1 and 3 μm made from film 2415-2. (b) The derivative $d(\mathrm{IDE})/(dI/I_{\rm dep})$ illustrating our approach to determining the beginning of the saturation plateau of detection efficiency and the value of detection current $I_{\rm det}$ of the sample. For $I_{\rm det}$ we take the bias current at which the derivative $d(\mathrm{IDE})/(dI/I_{\rm dep})$ has the maximum ($I_{\rm max}/I_{\rm dep}$). (c) Illustration that our approach is useful even if the saturation plateau is not observed: a dependence of internal quantum efficiency IDE on normalized bias current ($I/I_{\rm dep}$) measured at 1550 nm wavelength for the same three strips. (d) The derivatives $d(\mathrm{IDE})/(dI/I_{\rm dep})$ for the monotonically growing IDE presented in (c) exhibit clear maximum.

known DE (previously measured by precision positioning of the meander on a single-mode fibre pigtail).

For prevent 'latching' effect, we use small shunt resistors as we did it in our previous work [5]. The details of biasing with shunt resistor and its comparison with serial inductance we present here in section 5. We showed in our previous work that the use of the shunt leads to a certain increase in the observed value of the critical current $I_c^{\rm sh}$ compared to the critical current $I_{\rm c}$ measured without the shunt. We attribute this effect to a simple current division between the shunt and normal-metal wiring of the sample contacts. Everywhere in further presentation and discussion in this paper, if for a particular sample the currents are measured with the shunt, we reduce their values by a factor $I_c^{\rm sh}/I_{\rm c}$ measured for that particular sample to make them consistent with the measurements performed without shunts.

The density of the depairing current (actually, depearing current $I_{\rm dep}$ normalized to strip width w) at a given temperature $j_{\rm dep}(T)$ is calculated using the expression from [14]:

$$j_{\rm dep}(T) = 0.74\frac{[\Delta(0)]^{3/2}}{eR_s\sqrt{\hbar D}}\left[1-(T/T_{\rm c})^2\right]^{3/2}, \qquad (1)$$

where $\Delta(0)$ is superconducting gap at 0 K, e is electron charge, $R_{\rm s}$ is the sheet resistance, D is the diffusivity. For $\Delta(0)$ we use BCS formula $\Delta(0) = 1.76k_{\rm B}T_{\rm c}$ and we take $D = 0.4\,\mathrm{cm^2\,s^{-1}}$ which is typical for NbN. The use of equation (1) is justified by measurement of depairing currents in MoSi and NbN strips by Frasca *et al* [15].

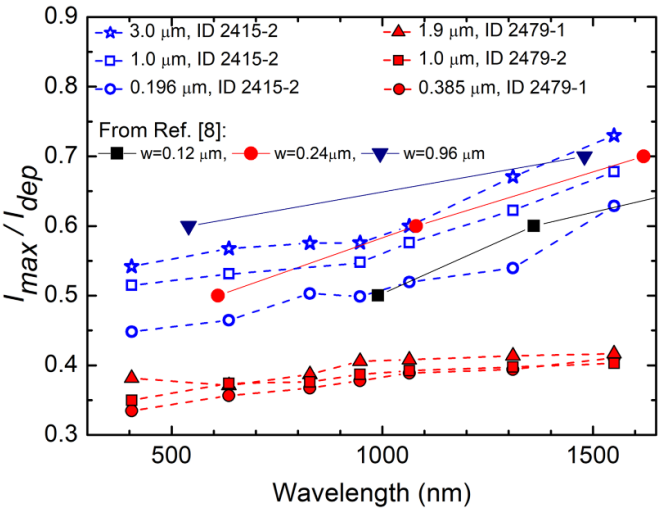

Figure 2. The values of $I_{\rm max}/I_{\rm dep}$ for strips with different width made from films 2415-2 and 2479 with $R_{\rm s}$ 550 and 625 $\Omega\,\mathrm{sq^{-1}}$ respectively. As a comparison, we also added several points taken from figure 11 of [8]. With the decrease of $R_{\rm s}$ the shift $I_{\rm max}/I_{\rm dep}$ with the wavelength and strip width becomes more pronounced.

3. Micron-wide strips

First, we study how the properties of the film result in the saturation of the quantum efficiency with the increase of the wavelength. For quantitative analysis we follow an approach presented in [16]: we attribute the beginning of the saturation plateau to the maximum of the derivative of the internal detection efficiency $d(IDE)/d(I/I\mathrm{dep})$. The procedure is illustrated by figure 1. The advantage of this method is that we can judge how close we are to the beginning of the plateau even if the plateau itself is not clearly observed yet (like shown in figures 1(c) and (d)). The resulting values of bias current $I_{\rm max}/I_{\rm dep}$ correspond to the maximum of the derivative, and also correspond roughly to the 'detection' current $I_{\rm det}$ in terms of Vodolazov paper [8].

Figure 2 shows $I_{\rm max}/I_{\rm dep}$ for strips with width in the range from 0.2 to 3 μm fabricated from two films with $R_{\rm s} = 550\,\Omega\,\mathrm{sq^{-1}}$ (film 2415-2, blue symbols) and $625\,\Omega\,\mathrm{sq^{-1}}$ (film 2479, red symbols). We can observe here that with the increase of the wavelength $I_{\rm max}/I_{\rm dep}$ shifts to higher values similar to what is predicted by Vodolazov [8]. For easier comparison, we added several relevant points from figure 11 of [8]: black squares corresponding to strip width 0.12 μm, red circles to width 0.24 μm, and black down triangles to width 0.96 μm. Although qualitatively experimental points for $R_{\rm s} = 550\,\Omega\,\mathrm{sq^{-1}}$ correspond to the theory, our experimental values of detection currents ('$I_{\rm max}/I_{\rm dep}$' in our terms) are smaller for all strip widths.

The deviation from the theory is even more pronounced for $R_{\rm s} = 625\,\Omega\,\mathrm{sq^{-1}}$: for all wavelength $I_{\rm max}/I_{\rm dep}$ is almost equal and is in range 0.3–0.4, not covered at all by the numerical simulation of [8]. Moreover, extrapolation of the theoretical data from figure 11 to such low $I_{\rm max}/I_{\rm dep}$ would result in visible range photons, whereas in the experiment photon wavelength reaches up to 1550 nm. Interestingly, in figure 11 of [8] higher

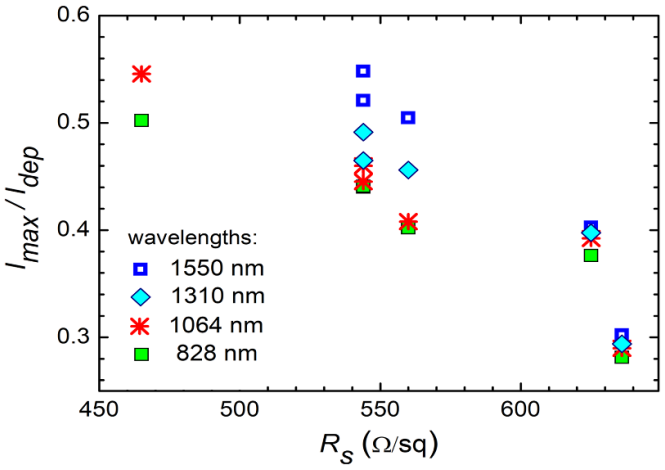

Figure 3. Dependence of I_{max}/I_{dep} on R_s for 1 μm-wide strips at wavelengths 800–1550 nm.

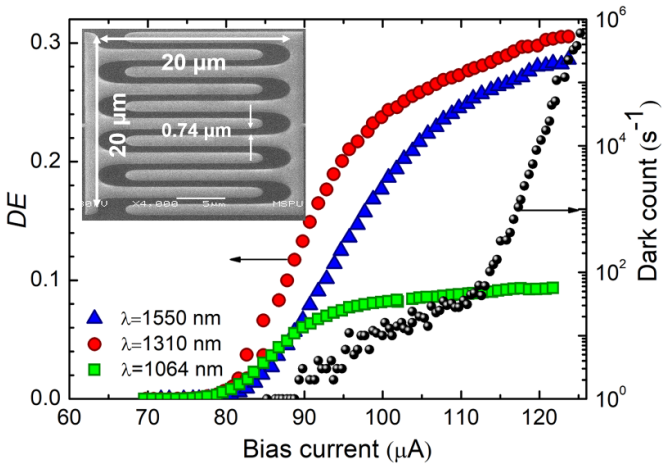

Figure 4. Detection efficiency DE and dark counts rate DC (black circles, right axis) vs bias current for 20 × 20 μm^2 meander from made from film 2474-1. Strip width is 0.74 μm. Plateaus are observed up to 1550 nm wavelength.

energy photons result in larger spread of I_{det}, whereas in our experiment there is almost no spread in I_{max}/I_{dep} for films with R_s higher than 600 Ω sq^{-1}.

Figure 3 presents the dependence of I_{max}/I_{dep} on R_s for 1 μm-wide strips from different films measured at wavelength in range from 800 to 1550 nm. With the decrease of R_s the spread of I_{max}/I_{dep} for photons of different energies increases, together with the increase of I_{max}/I_{dep}. Ultimately, for $R_s < 500$ Ω sq^{-1} the value I_{max}/I_{dep} approaches or even exceeds the critical current I_c of the strip. In this case the plateau of detection efficiency of course is not observed. From figure 3 one can conclude that for practical realization of SMSPD with the saturated detection efficiency films with $R_s > 600$ Ω sq^{-1} are more preferable. Such films feature a wide plateau in IDE curve for wavelengths from visible to 1550 nm.

4. Large-area meanders for applications

In order to estimate the ultimate characteristics of the large-area detectors suitable for multimode fibre coupling and free space we fabricated a number of meander-shaped samples with strip width in the range 0.35–1 μm covering areas 20 × 20, 50 × 50 μm^2, and meanders filling circular area 50 μm in diameter. The turns of the strip are designed according to equations (58) and (59) from [13] to reduce current-crowding effect. The SEM-images of such detectors are shown in the insets of figures 4 and 5.

Figure 4 presents detection efficiency (DE) and dark counts rate (DC) measured for 20 × 20 μm^2 meander made from film 2474-1 with $R_s = 636$ Ω sq^{-1}. The measurement is performed in a cryoinsert as described above in section 2. This meander has the strip width 0.74 μm and filling factor 35% exhibits plateaus in DE for all wavelength up to 1550 nm. The difference in DE for different wavelengths is caused by the Si_3N_4 sublayer acting as a cavity.

Figure 5(a) presents DE of the meander fabricated from film 2818 ($R_s = 676$ Ω sq^{-1}) and packaged with multi-mode fibre.

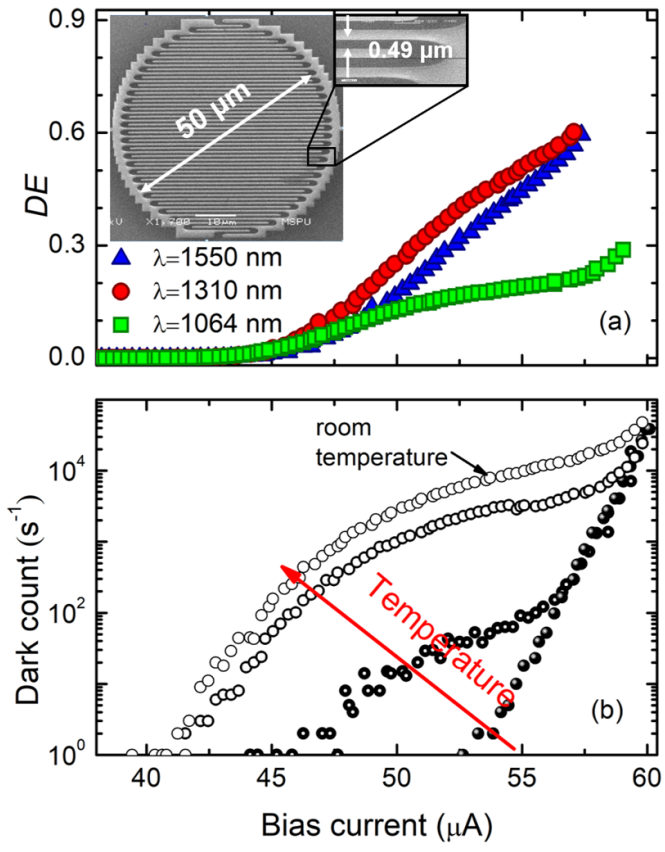

Figure 5. Detection efficiency (a) and dark counts rate (b) for circle-shaped detector with a diameter of 50 μm made from film 2818 with $R_s = 676$ Ω sq^{-1} and strip width 0.49 μm and measured on multi-mode fibre with 50 μm core diameter. Although plateau is observed only at 1064 nm wavelength, at 1310 and 1550 nm *DE* reaches 60%. High dark counts rate is caused by the thermal background photons which are not filtered by the multi-mode fibre: when input of the fibre is sufficiently cooled down, dark counts become purely exponential.

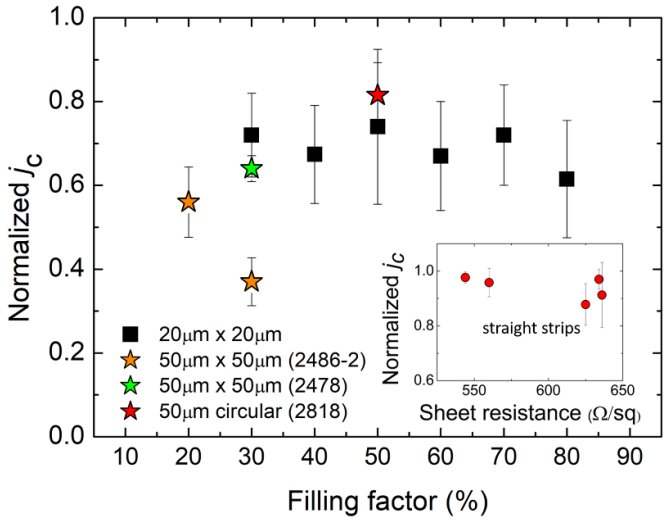

Figure 6. Statics of normalized critical current density j_c for meanders with different filling factors and for straight strips (in the inset). The points denote average values of j_c, error bars are the standard deviations. The statistics demonstrates that j_c reduction is caused by the size of meander rather than the filling factor suggesting that the current crowding in these devices is sufficiently eliminated.

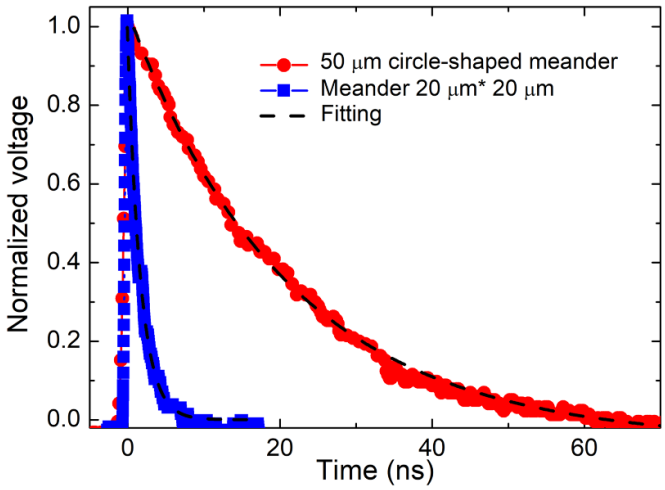

Figure 7. Waveform transients demonstrate kinetic-inductance-limited exponential decay of the falling edges for meanders of different size: 1.7 ns for 20 × 20 μm^2 (film 2474-1) and 20 ns for 50 μm circle-shaped meander (film 2818).

For this meander strip width is 0.49 μm and filling factor 50%. At wavelength 1064 nm saturated plateau is visible. At telecom wavelengths of 1310 and 1550 nm the saturation is not observed but yet DE reaches 60%. We attribute the absence of the saturation with the I_c limited by the defects (see also discussion of figure 6 below). Dark count rate for this detector is presented in figure 5(b). To check the contribution of thermal photons to the dark counts, we cooled down the top of the dipstick (together with the input of the fibre) with liquid nitrogen and recorded count rate at different temperatures while the dipstick was warming up to room temperature. At maximum cooling the count rate is purely exponential, while with the increase of the temperature it becomes like a photon-counting one.

Efficient coupling to optical fibre requires making the superconducting strip in a shape of either a spiral or meander. The spiral eliminates the current crowding almost completely (see e.g. very recent demonstration in [12]). On the other hand, in the center of the spiral where light intensity usually is maximal there is a blind spot where the 'sleeves' of the spiral turns around.

We focused on traditional meander shapes in a hope that proper design of the strip turns according to [13] will reduce current crowding and a loss in absorption due to unavoidable low filling factor can be compensated by a proper cavity design. Besides, long saturation plateau of DE also eliminates the problem of current crowding as it happens in traditional narrow-strip meanders with high filling factors.

Nevertheless, we accumulated the statistics of switching currents for all fabricated straight strips and meanders. For each batch we normalized critical current density j_c of all devices to the j_c of the straight strip with the maximum j_c, and then calculated average normalized j_c and standard deviation for the meanders as a function of filling factor. The result is presented in figure 6. The points denote average values of normalized j_c, the error bars denote the standard deviations. Surprisingly, the reduction of j_c does not depend on the filling factor in the whole range 20%–80%. On the contrary, it seems that the size of the meander (i.e. the length of the strip) plays a major role: large meanders covering area of 50 μm × 50 μm have smaller j_c in spite of low filling factor of 20% and 30%. The circular meanders from batch 2818 (like the one presented in figure 5 deviate from the general statistics. We attribute this 'success' to two factors: (a) only two such detectors were fabricated in this batch and they may happen to be very good accidentally, and (b) circular meanders have strip length reduced by about 20% compared to 'square' meanders which also helps to produce better devices. For comparison, we plotted j_c statistics for straight strips as well (in the inset).

For practical applications such as quantum computing and quantum cryptography timing characteristics of a detector are important. Figure 7 shows the comparison of photo-response voltage pulses for the shown above meanders. The kinetic-inductance-limited characteristic decay (by $1/e$) times τ_{exp} are 1.7 ns for 20 × 20 μm^2 from 2474-1 and 20 ns for 50 μm circle-shaped meander from 2818.

Another important characteristic is the timing jitter. We use 1064 nm pulsed laser and time tagger by Swabian Instruments to characterize the timing jitter of both meanders. The details of jitter measurement are described in [17]. The results are shown in figure 8. Both curves represent probability distribution function PDF of the photoresponse appearance at a given moment of time, and are measured at currents close to the critical current, namely $I/I_c = 0.98$ for meander 20 × 20 μm^2 and $I/I_c = 0.88$ for 50 μm circle-shaped meander.

Our previous study of the timing jitter in wide strips [17] shows that the shortest jitter is achieved at currents corresponding to the plateau of DE while in the region of growing DE (near I_{max}/I_{det}) the PDF curve is much longer, has non-Gaussian shape, often with several peaks. Such behavior can

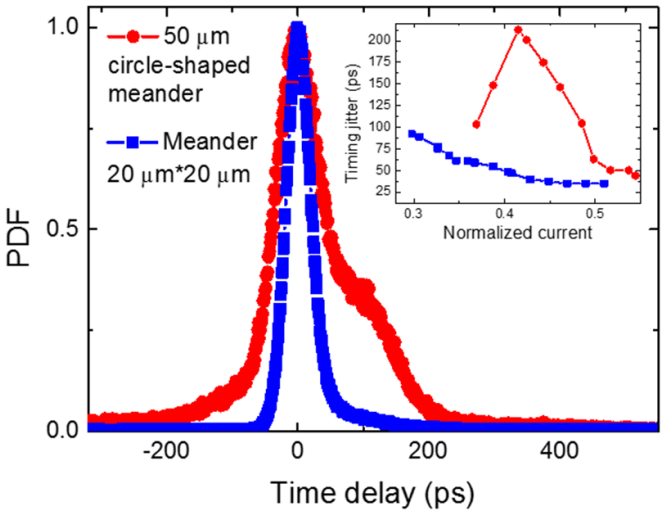

Figure 8. Probability distribution function PDF of photoresponse (timing jitter) for 50 μm circle-shaped meander (red) and 20×20 μm^2 meander (blue). The former demonstrates non-Gaussian shape similar to those we previously observed for wide strips [17]. The inset shows the dependence of timing jitter on bias current for both these devices.

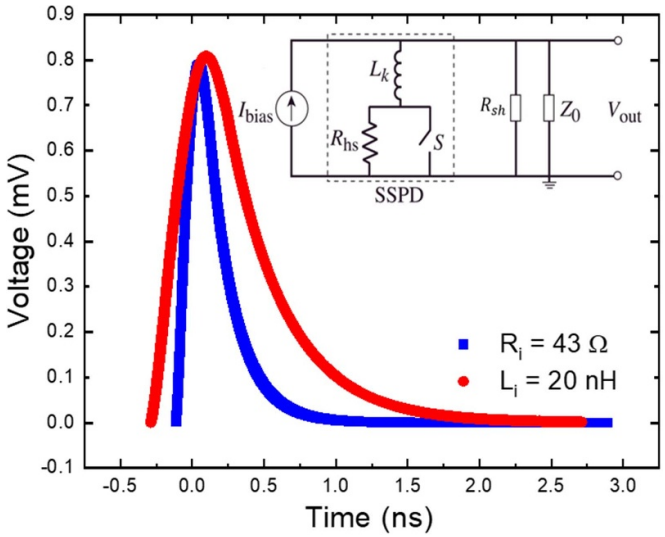

Figure 9. Comparison of the voltage pulse when using a shunt resistor and a series-connected inductance that does not lead to detector latching. Having almost the same amplitudes the pulse with the inductance in series is almost twice longer which makes the circuit with the shunt resistor more desirable for applications when timing jitter is important. The inset shows the equivalent circuit of the SMSPD using a shunt resistor in parallel to coaxial line.

be explained by the dependence of time required for vortex-antivortex pair to cross the strip on the bias current and the position where photon is absorbed [18].

We define the system jitter as the FWHM of the PDF and study its dependence on the bias current for both meanders. To arrange both curves on one graph we normalized bias current to depearing current. We subtract instrumental and noise contributions from system jitter and present the dependence of the timing jitters on the normalized current in the inset of figure 8. For circle-shaped meander we observe maximum on the timing jitter dependence on the bias current. It is connected with strongly non-Gaussian shape of the PDF in the range of normalized current 0.38–0.46 (like in [12, 17]). For meander 20×20 μm^2 the timing jitter dependence on normalized current is monotonic. The PDFs for this meander also have 'shoulder' at bias current less than I_{det}, but they are located lower than FWHM and do not make contributions to jitter. The minimal values of timing jitters are 44 ps for circle-shaped meander and a little bit lower for 20×20 μm^2 meander (34 ps) due to its lower kinetic inductance.

5. Biasing and read-out with shunt resistors

The use of SMSPDs leads to 'latching' [19] of the detector, i.e. the superconducting state is not restored after absorption of a photon. The solution to this problem is to slow down current in the strip which can be achieved either by a series inductance or a shunt resistor in parallel to the coaxial line. The resistor reduces the impedance (see inset in figure 9) which leads to a redistribution of currents, that is, a decrease in the current in the superconductor and the recovery of the superconducting state. Further, we consider the 'ideal' value of the shunt resistance to be the maximum value that does not lead to latching. On the other hand, it is more common to use series-connected inductance to prevent latching [10]. We will consider the value of the additional inductance 'ideal' if it is the minimum value that does not lead to latching.

For the calculation of 'ideal' shunt resistor or inductance one may use the electrothermal model describing the evolution of a normal domain based on solving the following differential equations [20]:

$$\frac{\partial cT}{\partial t} = J^2\,\rho + k\frac{\partial^2 T}{\partial x^2} - \frac{\alpha}{d}(T - T_{\rm sub}), \tag{2}$$

$$L_k\frac{\partial I}{\partial t} = IR_{\rm hs} - (I_{\rm bias} - I)Z_0, \tag{3}$$

here c is the heat capacity, J is the current density, ρ is the resistivity, k is the coefficient of thermal conductivity of the superconductor, α is the coefficient of thermal conductivity between the superconductor and the substrate, d is the thickness of the superconductor, $T_{\rm sub} = 1.7K$ is the substrate temperature, $L_{\rm k}$ is the kinetic inductance of SNSPD, $R_{\rm hs}$ is the resistance of the hot-spot, $I_{\rm bias}$ is bias current, Z_0 is the impedance of the coaxial line with shunt resistor. This electrothermal model was tested for the detectors based on wide superconducting strips [21]. Figure 9 illustrates the comparison of the voltage pulses in case of ideal shunt resistor and inductance. A sample with the following parameters was used for modeling: $d = 4.8$ nm, superconducting strip length $l = 10$ μm, superconducting strip width $w = 1$ μm, film sheet resistance $R_{\rm s} = 579\ \Omega\,{\rm sq}^{-1}$, critical temperature $T_{\rm c} = 10$ K.

The model gives the maximum value of the shunt resistance $R_{\rm sh} = 43\ \Omega$, the use of which does not lead to latching of the detector. One may use a smaller resistor, but a decrease

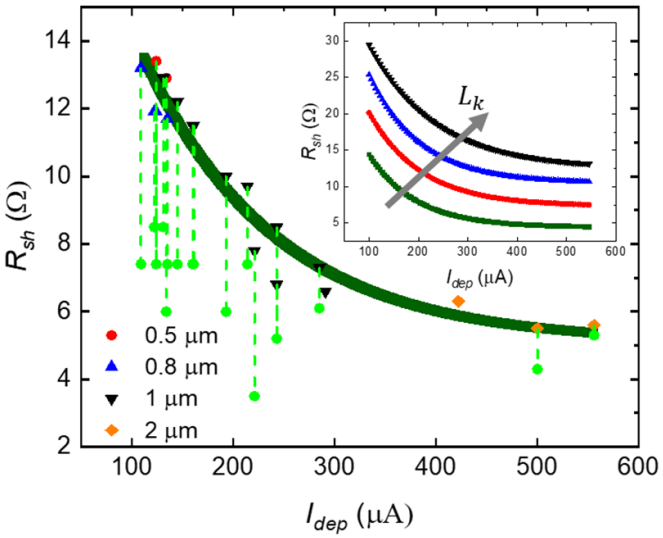

Figure 10. Comparison of the theoretically calculated maximum shunt resistance values (indicated by triangles) with those used in the experiment for NbN strips of different lengths. Each triangle is a calculated optimal shunt corresponding to a certain sample. Green circles are shunt values used in experiment and preventing latching. In many cases we did not strive to find the maximum possible value. The inset shows the change in the dependence of the shunt resistance on the device current when the sample inductance changes from L_k to $L_k \times 4$, respectively.

in shunt resistance leads to a decrease in the amplitude of the voltage pulse, which may reduce signal-to-noise ratio and increase jitter. So, with a shunt resistance value of $R_{sh} = 6.4\ \Omega$, the voltage pulse height was 0.3 mV.

The voltage pulse height when using an ideal series-connected inductance is slightly higher than when using an ideal shunt but the pulse with the serial inductance is almost twice longer. The increase in the time of the rising edge of the pulse should result in higher value of timing jitter, thus the use of shunt resistor seems more preferable for applications where jitter is critical.

Figure 10 sums up the experimentally used values of shunt resistor that prevents latching in straight 10-squares-long strips. The kinetic inductance of all samples is approximately the same and is equal to $L_k \approx 10^{-9}$ H. Other characteristics used for modelling such as thickness of the NbN film, critical temperature, sheet resistance, geometric dimensions, and depairing current are taken for each sample separately.

Each triangular point in figure 10 is the calculated maximum value of the shunt resistance for each sample. Different direction of the triangles and color means different widths of the superconducting strips ranging from 0.5 to 2 μm. Each triangle is connected by a dotted line with the respective experimental result (green circle). We did not always have an opportunity to adjust the optimal experimental shunt with the accuracy better than 2–4 Ω.

An exponential dependence of the required shunt resistance on the value of the depairing current is observed (green line is the exponential fit of the calculated values). The inset shows the dependence of the theoretically calculated shunt resistances on the depairing current for different sample kinetic inductances starting with L_k and increased with the step also equal to L_k. A linear dependence on inductance is observed.

6. Conclusion

We have investigated the influence of sheet resistance R_s on the single-photon detection capability of NbN strips with the width in the range 0.2–3 μm. We observe that (a) the length of the DE saturation plateau decreases with the decrease of photon energy which is in agreement with Vodolazov's explanation of detection mechanism, and (b) for films with R_s higher than 630 Ω the saturation plateau of DE starts at I/I_{dep} in range 0.3–0.4 and almost does not depend on strip width and photon energy. Overall experimental results show that the optimal R_s should be greater than 630 Ω sq^{-1} for a clearly observable saturation of DE at wavelengths above 1 μm.

We fabricated and characterized meander-shaped detectors with strip widths 0.49 and 0.74 μm and covering areas in shape of circle with a diameter 50 μm and in shape of 20 × 20 μm^2 square which are feasible for multi-mode fibre and free space coupling. The meander with 0.49 μm-wide strip exhibits DE up to 60%. We also demonstrated that being multi-mode fibre coupled such meanders are sensitive to thermal background photons causing the excess dark count rate.

Finally, we used electro-thermal feed-back model to compare additional inductor vs a shunt resistor as counter-latching measures. Providing the same amplitudes, shunt resistor gives a pulse with shorter time constant which might be more favorable for achieving ultimate jitter. We also demonstrated reasonable agreement between the calculated optimal values of shunt resistors and those used in the experiment.

Data availability statement

The data that support the findings of this study are available upon reasonable request from the authors.

Acknowledgment

The work was supported by the Russian Foundation for Basic Research (RFBR) Grant No. 18-29-20100 (in part of NbN films and straight strips fabrication and characterization), and the Russian Science Foundation (RSF) Grant No. 20-12-00287 (in part of meander characterization). We thank Swabian Instruments GmbH and Dr Helmut Fedder personally for the kindly provided experimental equipment (Time Tagger Ultra 8).

ORCID iDs

Yu P Korneeva https://orcid.org/0000-0003-1576-265X
M A Dryazgov https://orcid.org/0000-0002-6280-4667
Ph I Zolotov https://orcid.org/0000-0003-1729-7480
A A Korneev https://orcid.org/0000-0002-0116-9591

References

[1] Holzman I and Ivry Y 2019 Superconducting nanowires for single-photon detection: progress, challenges and opportunities *Adv. Quantum Technol.* **2** 1800058

[2] Reddy D V, Nerem R R, Nam S W, Mirin R P and Verma V B 2020 Superconducting nanowire single-photon detectors with 98% system detection efficiency at 1550 nm *Optica* **7** 1649

[3] Peng H *et al* 2020 Detecting single infrared photons toward optimal system detection efficiency *Opt. Express* **28** 36884–91

[4] Zadeh I E *et al* 2020 Efficient single-photon detection with 7.7 ps time resolution for photon-correlation measurements *ACS Photonics* **7** 1780–7

[5] Korneeva Y P, Yu Vodolazov D, Semenov A V, Florya I N, Siminov N, Baeva E, Korneev A A, Goltsman G N and Klapwijk T M 2018 Optical single-photon detection in micrometer-scale NbN bridges *Phys. Rev. Appl.* **9** 064037

[6] Zotova A N and Vodolazov D Y 2012 Photon detection by current-carrying superconducting film: a time-dependent Ginzburg–Landau approach *Phys. Rev.* B **85** 1–9

[7] Zotova A N and Yu Vodolazov D 2014 Intrinsic detection efficiency of superconducting nanowire single photon detector in the modified hot spot model *Supercond. Sci. Technol.* **27** 125001

[8] Vodolazov D Y 2017 Single-photon detection by a dirty current-carrying superconducting strip based on the kinetic-equation approach *Phys. Rev. Appl.* **7** 034014

[9] Korneeva Y P, Manova N N, Florya I N, Mikhailov M Y, Dobrovolskiy O V, Korneev A A and Vodolazov D Y 2020 Different single-photon response of wide and narrow superconducting $Mo_x Si_{1-x}$ strips *Phys. Rev. Appl.* **13** 024011

[10] Charaev I, Morimoto Y, Dane A, Agarwal A, Colangelo M and Berggren K K 2020 Large-area microwire MoSi single-photon detectors at 1550 nm wavelength *Appl. Phys. Lett.* **116** 242603

[11] Chiles J *et al* 2020 Superconducting microwire detectors based on WSi with single-photon sensitivity in the near-infrared *Appl. Phys. Lett.* **116** 242602

[12] Guangzhao X *et al* 2021 Superconducting microstrip single-photon detector with system detection efficiency over 90% at 1550 nm *Photon. Res.* **9** 958–67

[13] Clem J R and Berggren K K 2011 Geometry-dependent critical currents in superconducting nanocircuits *Phys. Rev.* B **84** 174510

[14] Clem J R and Kogan V G 2012 Kinetic impedance and depairing in thin and narrow superconducting films *Phys. Rev.* B **86** 174521

[15] Frasca S *et al* 2019 Determining the depairing current in superconducting nanowire single-photon detectors *Phys. Rev.* B **100** 054520

[16] Smirnov K, Divochiy A, Vakhtomin Y, Morozov P, Zolotov P, Antipov A and Seleznev V 2018 NbN single-photon detectors with saturated dependence of quantum efficiency *Supercond. Sci. Technol.* **31** 035011

[17] Vodolazov D, Manova N N, Korneeva Y and Korneev A A 2020 Timing jitter in NbN superconducting microstrip single-photon detector *Phys. Rev. Appl.* **14** 044041

[18] Yu Vodolazov D 2019 Minimal timing jitter in superconducting nanowire single-photon petectors *Phys. Rev. Appl.* **11** 014016

[19] Annunziata A J *et al* 2010 Reset dynamics and latching in niobium superconducting nanowire single-photon detectors *J. Appl. Phys.* **108** 084507

[20] Yang J K W, Kerman A J, Dauler E A, Anant V, Rosfjord K M and Berggren K K 2007 Modeling the electrical and thermal response of superconducting nanowire single-photon detectors *IEEE Trans. Appl. Supercond.* **17** 581–5

[21] Dryazgov M, Semenov A, Manova N, Korneeva Y and Korneev A 2020 Modelling of normal domain evolution after single-photon absorption of a superconducting strip of micron width *J. Phys.: Conf. Ser.* **1695** 012195